Journal of Applied Physics

RESEARCH ARTICLE | SEPTEMBER 14 2022

Nanomechanical and tribological properties of nickel–chromium multilayer coating on Inconel 617

Special Collection: Advances in Multi-Scale Mechanical Characterization

Ayesha Asif ; Saifur Rahman ; Andreas A. Polycarpou

Journal of Applied Physics 132, 105305 (2022)
https://doi.org/10.1063/5.0098795

AIP Publishing

Journal of Applied Physics ARTICLE scitation.org/journal/jap

Nanomechanical and tribological properties of nickel–chromium multilayer coating on Inconel 617

Cite as: J. Appl. Phys. **132**, 105305 (2022); doi: 10.1063/5.0098795
Submitted: 12 May 2022 · Accepted: 16 August 2022 ·
Published Online: 14 September 2022

Ayesha Asif, Saifur Rahman, and Andreas A. Polycarpou[a)]

AFFILIATIONS

J. Mike Walker '66 Department of Mechanical Engineering, Texas A&M University, College Station, Texas 77843, USA

Note: This paper is part of the Special Topic on Advances in Multi-Scale Mechanical Characterization.
[a)]**Author to whom correspondence should be addressed:** apolycarpou@tamu.edu. **Tel.:** (979) 458-5763

ABSTRACT

Multilayer coatings of Ni and Cr were deposited onto Inconel 617, and multi-scale physical properties were characterized using high temperature tribological experiments, nanoindentation, and microscratch. The effect of high temperature aging (950 °C under helium environment) on two different Ni/Cr multilayer coatings with individual layer thicknesses of 50 and 200 nm denoted by Ni/Cr(50) and Ni/Cr(200) was investigated. Nanoindentation of original coatings showed a hardness of 6 GPa that increases to 14 GPa for both samples once aged. Microscratch results support the macro-tribology results where Ni/Cr(50) (without aging) was the only delaminated coating with significant wear. Additionally, aging in both cases reduced the *in situ* coefficient of friction and wear. Cross-section energy dispersive spectrometry confirmed that the aged oxide layer was two to three times thicker than the original coating. An abundance of chromium oxide was found in the main body of the coatings, which led to higher hardness and better wear resistance.

I. INTRODUCTION

Coatings have been used in several applications to improve contact performance and increase the service life of components. Multilayer coatings consist of pure metals, metal oxides,[1] and nitrides[2] with various individual layer thickness and material combinations to obtain desirable mechanical, thermal, and tribological properties. Multilayer coatings produced using the sputtering method can have homogenous layers and allow fine-tuning of the properties of the final coating by varying the individual layer thickness at the nanoscale.[1]

Ni and Cr metals have been previously combined with other metals such as Ag and Cu in multilayer systems.[1] In the case of the Ni/Cr coatings, the application here is to produce coatings that can provide protection in environmental conditions of very high temperature gas cooled reactors (VHTRs) where outlet temperatures can reach 900–1100 °C.[3] Generally, nickel-based alloys have been the prime choice for structural components in applications with high service temperatures such as nuclear reactors, steam turbines, and the aerospace industry where prolonged degradation can occur due to heat and corrosive environments.[3–5] Protective coatings can be considered a solution to prevent the loss of Cr from the surface of the alloy and form well-bonded oxide layers.

High temperature conditions are known to form protective hard oxide layers on nickel-based superalloys, but the effect on such a multilayered Ni/Cr coating is unknown. Previously, the nickel film has been used to prevent Cr evaporation from ferritic steels due to a Ni–Fe oxide scale formed after aging.[6] Studies on Inconel 617 and 800HT alloy have also shown hard Cr-oxide layers form within a few hours of aging in He and air.[7] The top Cr oxide-rich layer includes a mixed oxide sublayer with Al oxides along the grain boundaries.[8] Another study involved deposited oxide (Cr_2O_3) onto steel for improved tribological properties, strength, and toughness.[9] Due to the beneficial effects of the oxide layers, the aged behavior is of significance as metallic multilayer coatings placed in high temperature environment can form a protective oxide layer over Inconel without compromising friction and wear performance.

Due to the small-scale of multilayered coatings, it is necessary to investigate the multi-scale nano-, micro-, and macro-behaviors. Macroscale experiments involve high temperature tribology experiments compared with friction and wear behaviors of the coatings (before and after aging) at the macroscale.

The hardness is extracted from nanoindentation, and microscratch data are used to calculate the adhesive and shear strength of

the coatings,[10] which are compared to the tribological friction and wear at the macroscale.

This study uses Ni/Cr multilayer coatings of individual layer thickness of 50 and 200 nm deposited on the Ni-alloy (Inconel 617). Aging was performed at 950 °C for 10 h in helium to simulate high temperature gas cooled reactors (HTGRs) and VHTR conditions.[11] Surface morphology of pristine and aged coatings was observed via scanning electron microscopy (SEM). In addition, energy dispersive spectrometry (EDS) analysis of the oxide layer cross section was performed and used to provide explanations for the observed experimental behaviors.

II. EXPERIMENTAL PROCEDURE

A. Coating preparation

Ni/Cr multilayers with individual layer thicknesses of $h = 50$ nm and $h = 200$ nm were deposited on Si 110 and SiO_2 substrates for the preliminary fabrication process. The first coating denoted Ni/Cr(50) has individual Ni and Cr layers of 50 nm thickness resulting in a total coating of 1.5 μm total thickness, and the second coating denoted Ni/Cr(200) has an individual layer thickness of 200 nm and a total film thickness of 2 μm.

A bright-field XTEM micrograph of Ni/Cr(50) multilayer coating (on the Si 110 substrate) is shown in Fig. 1(a). The inset selected area diffraction (SAD) pattern clearly demonstrates the formation of the polycrystalline structure after deposition and no preferable texture is observed. The EDS mapping results [Fig. 1(b)] and its corresponding line profiles [Fig. 1(c)] verify the chemically alternating layer structure achieved through the coating deposition process.

For nanoindentation, microscratch, and macro-tribology experiments, Ni/Cr(50) and Ni/Cr(200) coatings were also deposited on Inconel 617 alloy substrates by direct current magnetron sputtering at room temperature. Before sputtering, the alloy substrates were mechanically ground and polished, followed by ultrasonic cleaning using ethanol. The sputtering chamber was evacuated to a base pressure of less than 5×10^{-8} Torr before deposition. In this multilayered structure, the first layer on the Inconel substrate is Cr and the topmost layer is Ni. For the coating samples deposited on the Inconel substrate, the cross-section SEM and EDS presented in Sec. II B was used to confirm the coating dimensions and elemental compositions before and after aging. For each experiment, one sample was used in the pristine condition (room temperature referred to as RT), and the second was aged at 950 °C in helium for 10 h. Both RT and aged samples were subjected to nanoindentation, microscratch, and tribological experiments.

B. EDS elemental mapping

Cross-section EDS of Ni/Cr(50)-RT and Ni/Cr(200)-RT samples are shown in Fig. 2. The coating thickness can be estimated from the images as 1.3 and 2.0 μm, respectively. The Ni/Cr (200) samples under EDS showed the structure of the alternating Ni and Cr layers, Fig. 2(b). After aging, the EDS mapping is shown in Fig. 3 for Ni/Cr(50)-aged and Ni/Cr(200)-aged. Aged samples were plated with Ni so any Ni appearing above the oxide layer is due to the plating, Fig. 3(a). Much of the top layer is a chromium oxide-rich region with uneven thickness, which fades into the Inconel substrate. After aging, Cr intensifies on the top layer and so does oxygen. Nickel has migrated away from the coating and is detected as pockets near the substrate. After aging for 10 h, the thickness of the CrO layer is between 2 and 4 μm for both samples. The chromium-rich layer contributes to the higher hardness of both Ni/Cr(50) and Ni/Cr(200). However, the porosity of the Cr oxide allows internal oxidation of some elements such as aluminum below the oxide. Both aged samples show aluminum oxide underneath the Cr-oxide layer. Such Cr-rich oxide layers with alumina have been reported in aged Inconel samples.[3,4,11] Higher Al content can result in more alumina growth near the surface oxide and Inconel interface. While alumina reduces the diffusion of cations providing some protection, a higher level of Al can cause poor mechanical behavior, low strength, and low creep resistance.[4] Alumina grows at the grain boundaries, eventually behaving as sites for fracture propagation. Having the multilayer of pure Ni/Cr reduces the aluminum content near the surface, possibly reducing the alumina growth, as compared to the bare Inconel alloy.

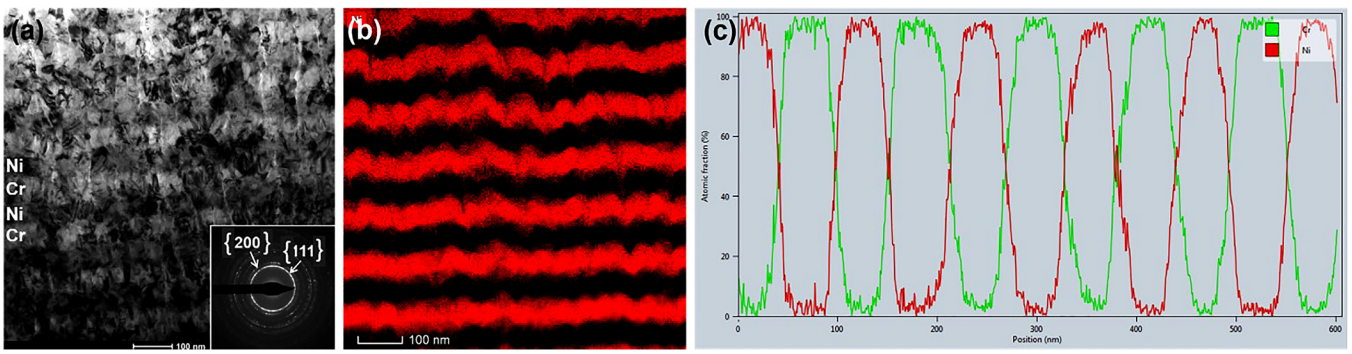

FIG. 1. XTEM micrograph of Ni/Cr(50) with a 50 nm multilayer showing the polycrystalline structure. (b) EDS mapping result of Ni and (c) corresponding line profiles verifying the chemically modulated multilayer structure.

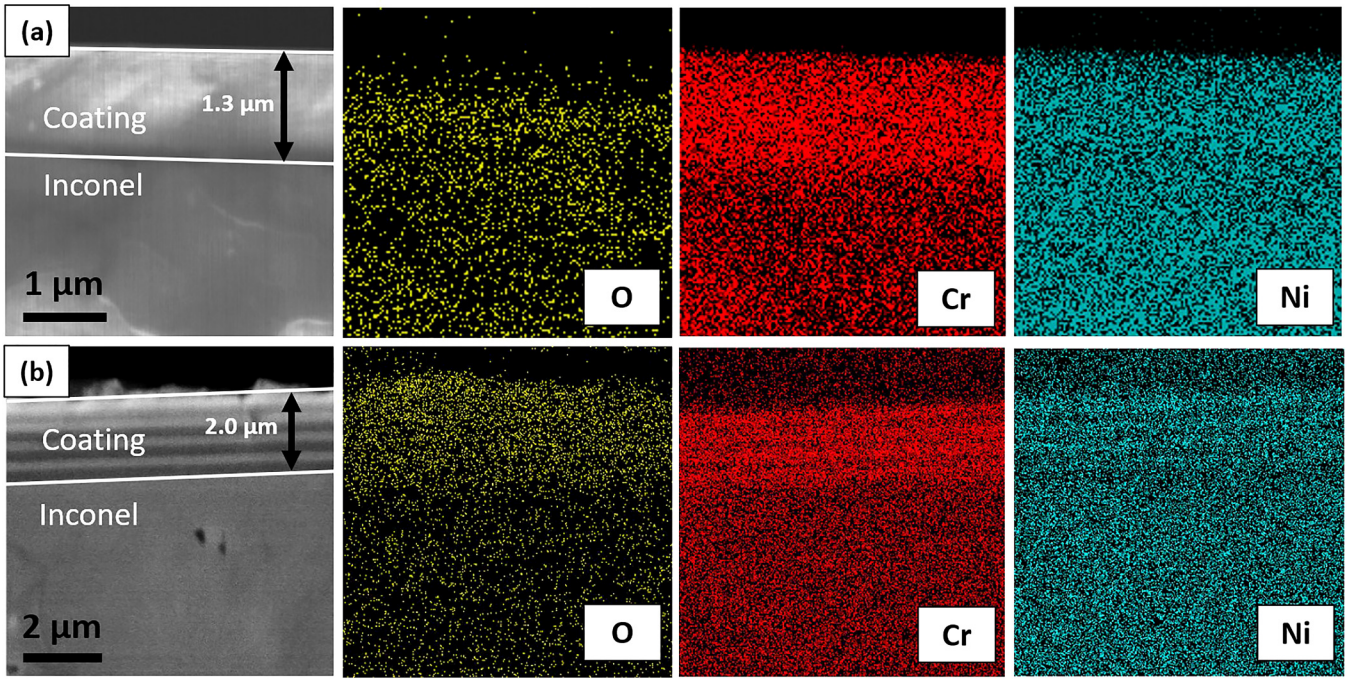

FIG. 2. Cross-section EDS elemental mapping of (a) Ni/Cr(50)-RT and (b) Ni/Cr(200)-RT.

C. Macro-tribological experiments

Ni/Cr(50) and Ni/Cr(200) multilayer coatings were tested using a specialized high temperature tribometer (HTT) with a ball-on-disk configuration. The coating is on the disk only and 6 mm diameter sapphire balls were used as the counterpart. The HTT is used to simulate environmental conditions of HTGR and VHTR with outlet temperatures of 700–950 °C. Three samples were used for each coating: The first is pristine coating tested at RT, the

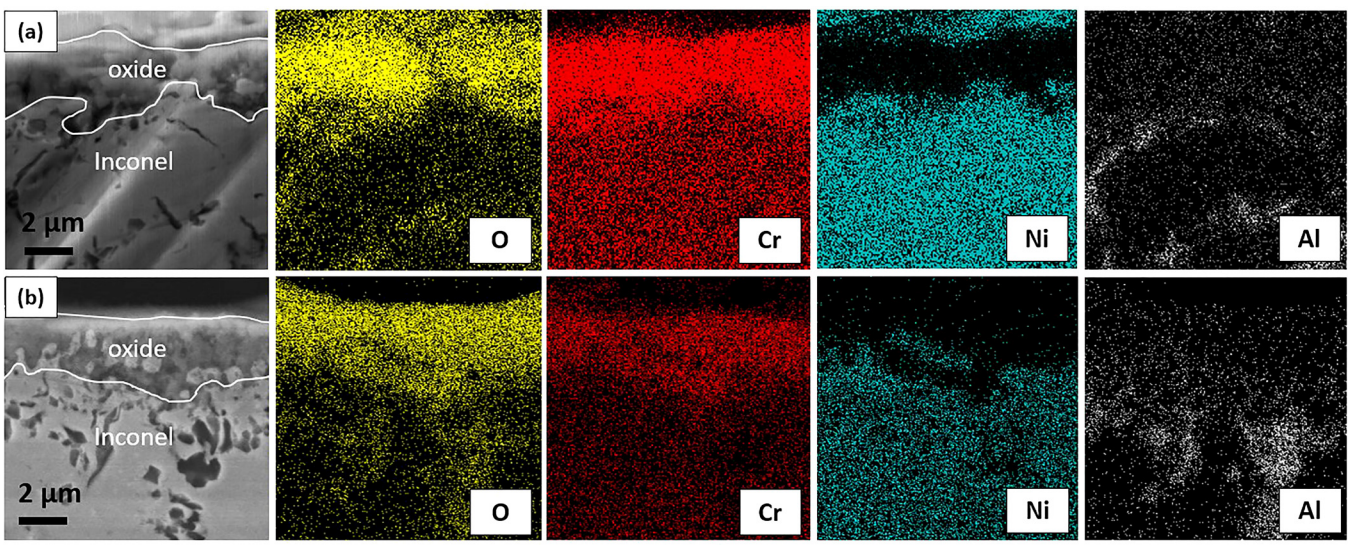

FIG. 3. Cross-section EDS elemental mapping of (a) Ni/Cr(50)-aged and (b) Ni/Cr(200)-aged.

second at a chamber temperature of 800 °C, and finally, the aged coating was tested also at 800 °C.

All experiments were performed under He environment, similar to the representative environments for HTGR/VHTR. The tribo-experiments were performed under a constant normal load of 3 N and a sliding velocity of 0.04 m/s for 10 min. The *in situ* coefficient of friction (COF) was measured and profilometry scans of the wear tracks on the coating were recorded to measure the exact amount of wear.

D. Nanoindentation and microscratch

The nanoindentation and microscratch experiments were performed using a TriboPremier nanoindenter (Bruker) with the high-load Omni probe transducer. The nanoindentation experiments were carried out using a Berkovich probe having a tip radius of 150 nm. Indentation load range of 10–15 mN was used for room temperature coatings and 15–30 mN for the aged coatings. The *in situ* indentation depth range for the data presented here was maintained at 150–200 nm, which is within 10% of the total coating thickness to reduce the influence of substrate effects. A series of at least 10 indents were used to calculate average hardness and reduced modulus values. For comparison with the multilayered structure, nanoindentation was also performed on pure Ni and pure Cr coatings (1.0 μm thickness).

A schematic of a typical load–displacement curve resulting from an instrumented indenter during indentation is depicted in Fig. 4. The load–displacement curves are used to extract the penetration depth (h_{max}), contact depth (h_c), and slope $\left(S = \frac{dP}{dh}\right)$ of the unloading curve. In order to calculate the hardness and reduced modulus, the area function of the probe must be calibrated to take into account the probe imperfections. Equation (1) defines the contact area (A_c) of the probe in terms of the contact depth (h_c) using the Oliver and Pharr method.[12] Coefficients C_1–C_5 are extracted by curve fitting using several indentations on a standard sample of known hardness. In this case, the standard sample was fused quartz with $H = 9.3$ GPa (±10%) and $E_r = 69.6$ GPa (±5%). Reduced modulus (E_r) is calculated using Eq. (2) using the slope $\left(S = \frac{dP}{dh}\right)$ of the initial portion of the unloading curve. The hardness [Eq. (3)] is obtained using the maximum load (P_{max}) and calculated contact area (A_c),

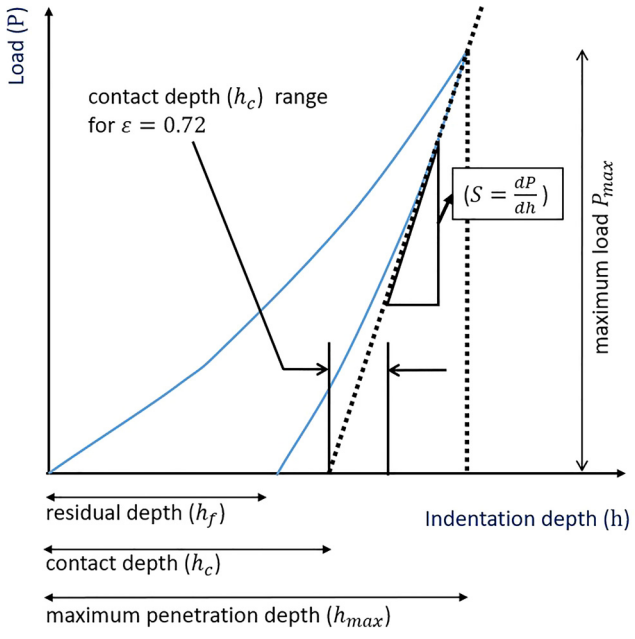

FIG. 4. Typical nanoindentation load vs displacement curve and the values to be extracted for hardness, H, and reduced modulus, Er.

$$A_c = C_o h_c^2 + C_1 h_c + C_2 h_c^{1/2} + C_3 h_c^{1/4} + C_4 h_c^{1/8} + C_5 h_c^{1/16}, \quad (1)$$

$$E_r = \frac{\sqrt{\pi}}{2\sqrt{A_c}} S, \quad (2)$$

$$H = \frac{P_{max}}{A_c}. \quad (3)$$

To measure the adhesion and shear strength values of the coatings, microscratch experiments were performed using a conospherical probe (tip radius 9.98 μm, as measured with an SEM) with the high-load Omni probe transducer. These experiments were intended to delaminate each coating from the substrate using a ramp load scratch of 100 μm length for a load range between 400 and 1200 mN with a constant linear scratch speed. Figure 5 shows a schematic of the scratch alongside the changing COF and application of the normal load vs lateral displacement. Loading involves a pre-scan at minimum preload, followed by the linearly increasing ramp loading scratch and the retrace (post-scan) step. The scratch was used to obtain values of P_c (critical load) and d_c (critical width) at the onset of failure (marked by an abrupt change in COF) for the calculation of σ_a (adhesive strength) and τ_c (shear strength) of the coatings before and after aging. The adhesive and shear strength calculations are detailed in Sec. III D. The initiation of failure was established through observing changes in friction, normal displacement, and observed failure characteristics elaborated in Sec. III D.

E. Characterization

The coating surfaces, scratch images, and cross-section SEM and EDS analyses were captured using a JOEL FE-SEM. The cross sections of the RT and aged samples were prepared for SEM imaging by embedding them into a conductive mold in a heated powder press and then polished to a mirror finish. Surface topography was measured using the scanning probe microscopy (SPM) feature of the indenter (and using the same Berkovich probe with the TI Premier nanoindenter). After the tribology experiments, the exact wear tracks were measured using a Dektak Profiler.

III. RESULTS AND DISCUSSION

A. Macro-tribological experiments

Experiments were performed using the HTT simulating HTGR/VHTR conditions. Three different experiments were

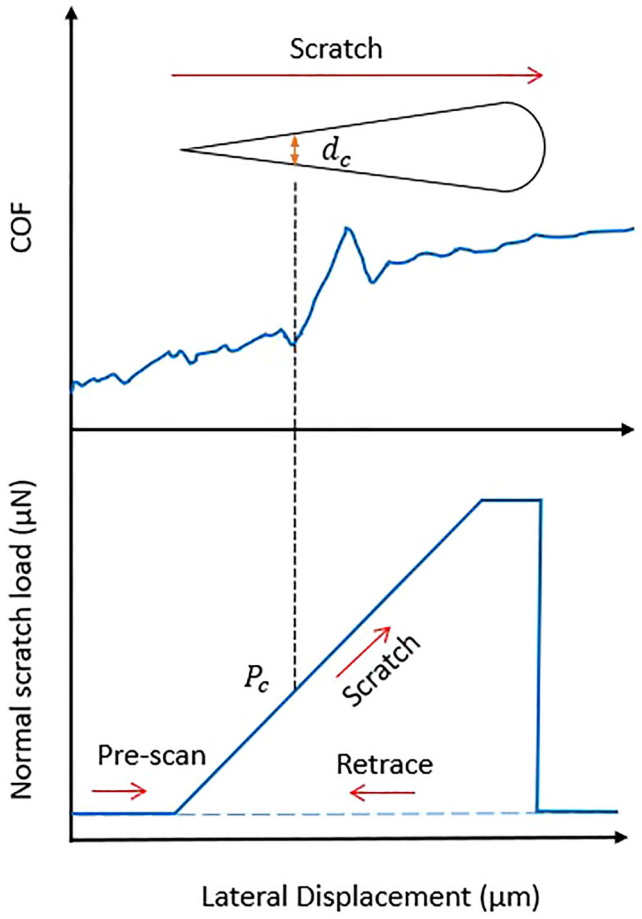

FIG. 5. Schematic of COF and normal load vs lateral displacement for a typical ramp load scratch. The diagram of the scratch shows where the critical load and width of the scratch are extracted.

performed for each multilayer coating [Ni/Cr(50) and Ni/Cr(200)] in the He environment: (i) RT experiments, (ii) 800 °C experiments for untreated RT samples, and (iii) 800 °C experiment for aged samples. Typical COF vs experimental duration and the corresponding profiler scans of the wear track on the disks are show/n in Fig. 6. The Ni/Cr(50) tested under RT resulted in very high and unstable COF throughout, averaging at 1.6 toward the last few minutes of the experiment [Fig. 6(a)]. Similarly, the wear is also high as the coating was delaminated entirely and the Inconel substrate underwent material loss as seen from the wear scar depth of almost 12 μm [Fig. 6(c)]. Aging Ni/Cr(50) has reduced the COF in the macro-tribological experiments to 0.7 and remained stable throughout the experiment. The wear scan [Fig. 6(c)] indicates that some coating removal does occur (2 μm wear depth) but did not result in complete delamination or sudden loss of the substrate material. Adhesive and shear strength values calculated in Sec. III D using microscratch indicate positive correlation with the tribological results.

The experiments on RT samples performed at 800 °C represent an intermediate stage between RT and aged samples, where the samples oxidize during the experiment. The COF and wear were comparable to the aged sample indicating the initiation of the hardened oxide layer has taken place rapidly and aging the samples for longer durations can further increase the oxide layer for better protective ability. The SEM image in Fig. S1 (in the supplementary material) shows Ni/Cr(50) after testing at 800 °C and that the growth of the spinel oxides has already occurred.

For Ni/Cr(200), the RT sample does show higher and more unstable COF with a mean value of 0.9 in the latter half of the experiment [Fig. 6(b)]. The wear of Ni/Cr(200)-RT differs from Ni/Cr (50)-RT such that Ni/Cr(200)-RT shows superior resistance to wear and wear scar depth is only 2 μm [Fig. 6(d)]. Thicker individual layers in the case of Ni/Cr(200) have allowed for better adhesion and reduced the likelihood of failure at the macroscale. The COF for aged and RT samples of Ni/Cr(200) at 800 °C, both show lower COF of 0.7 and 0.6, respectively, towards the completion of the wear test. The wear behavior in this case is very similar to the RT experiment. Comparatively, the *in situ* COF for 800 °C experiments was less than the COF of 1.4 on measured on bare Inconel 617 tested under similar conditions.[11] The aging process fused the individual Ni and Cr layers, resulting in a harder and thicker overall coating on the Inconel substrate. The indentation and scratch data are needed to reveal the hardness and adhesion strength. The improvement of nanoscale adhesion and shear strength properties of aged samples can directly influence macroscale behavior, reducing COF and increasing wear resistance.

B. Surface morphology

The top surface SEM images of the untested coatings are presented in Fig. 7. The Ni/Cr(50)-RT and Ni/Cr(50)-aged samples are shown in Figs. 7(a) and 7(b) and the Ni/Cr(200)-RT and Ni/Cr (200)-aged samples are shown in Figs. 7(c) and 7(d), respectively. The overall grain size and roughness of Ni/Cr(50)-RT is lower (<100 nm) than that of Ni/Cr(200)-RT, which exhibits a grain size of up to 100 nm, as in Figs. 7(a) and 7(c). The smaller grain size of Ni/Cr(50)-RT is expected to strengthen the film by hindering dislocation motion and the propagation of cracks.[2] The dislocations pileup at the grain boundaries, which are more abundant with smaller grain size lead to Hall–Petch strengthening.[2,13] After aging at 950 °C for 10h, spinel oxides have developed on the surface of both samples. The size of spinels on Ni/Cr(50) is larger varying in thickness between 100 and 500 nm [Fig. 7(b)]. Thinner individual layers of Ni/Cr(50) allow for quicker diffusion of elements across the coating, allowing the aging to progress rapidly and producing larger spinel structures. For Ni/Cr(200) [Fig. 7(d)], the spinels appear abundant; however, the size range is lower (100–200 nm or less), compared to Ni/Cr(50)-aged. The roughness is directly influenced by the spinel and grain growth on the top surface. Root mean square roughness, R_{rms}, was obtained for the coating samples (RT and aged) using Scanning Probe Microscopy (SPM) imaging (scan size of 10 μm) and the measured roughness values are shown in Table I.

C. Nanoindentation

Nanoindentation was performed on each sample, and the hardness and reduced modulus values were extracted using the

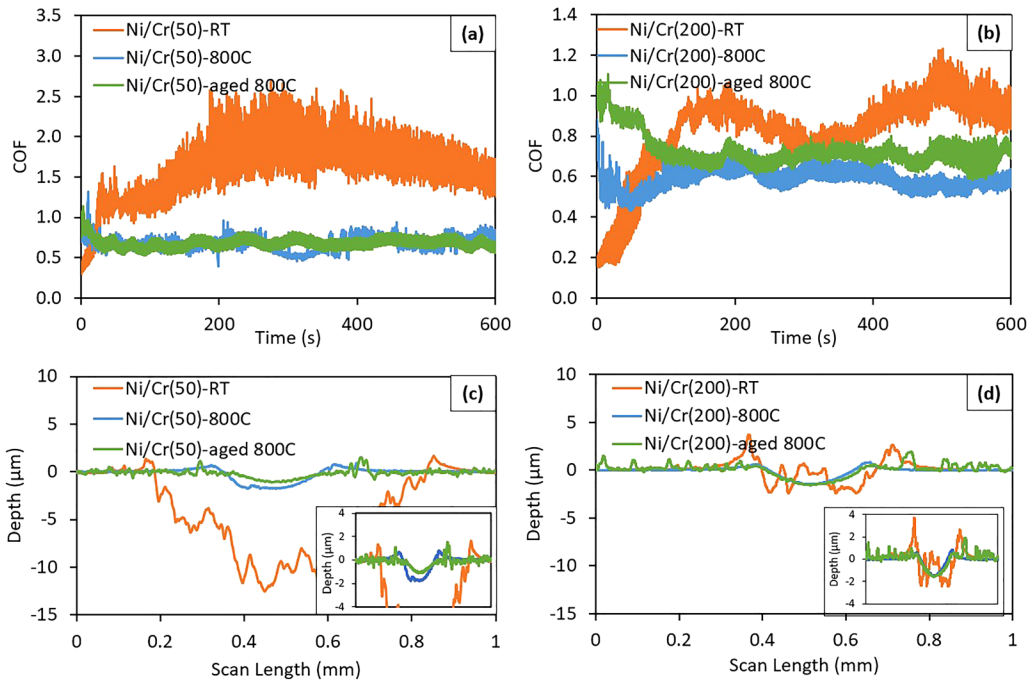

FIG. 6. *In situ* COF of (a) Ni/Cr(50), (b) Ni/Cr(200) in He under 3 N normal load and sliding velocity of 0.04 m/s and corresponding wear scar profiler scans of (c) Ni/Cr (50), (d) Ni/Cr(200).

Oliver and Pharr method. Table I summarizes the samples investigated and the properties measured. The overall thickness measurements of the RT and aged coatings were measured directly from cross-section SEM/EDS images (Sec. II B). Pure Ni and Cr coatings (on silicon wafer substrates) were also included in nanoindentation to compare with the hardness of the constituent elements deposited with the same method. It is evident that both multilayer coatings had an overall higher hardness than the coatings made of constituent elements Ni and Cr. The hardness measured on Ni/Cr(50)-RT was 6.62 ± 0.89 GPa, and Ni/Cr(200)-RT sample hardness was 5.90 ± 0.13 GPa. The indentation contact depth was maintained at an average 150 nm for Ni/Cr(50) and 200 nm and Ni/Cr(200), which is within 10% of the total coating thickness to avoid the effect of the rigid Inconel substrate. After the aging process, hardness doubles for both coatings (approximately 14 GPa) and reduced modulus increases by 43% and 19% for Ni/Cr(50) and Ni/Cr(200), respectively.

In a nanoindentation study of CrO deposited on glass substrates, the hardness is reportedly in the range of 12–22 GPa and reduced modulus in the range of 76–180 GPa.[14] This indicates that the oxide layer in these multilayer samples is expected to be predominantly CrO that contributes to the overall hardness. The increase in hardness is attributed to the oxidation layer becoming thicker and the migration of Ni out of the main oxide layer of the coating (confirmed by EDS). The overall thickness for Ni/Cr(50) increased by a factor of 2.5 while the Ni/Cr(200) oxide layer increased the coating thickness by a factor of 2. It is possible that in the case of Ni/Cr(50), the thinner individual layers allowed for quicker diffusion of elements across the coating. It has been reported for the oxide layer of Cr that the oxygen flow rate has an optimal value and can impact the resulting structure of the oxide.[9] A higher oxygen flow rate can result in the larger grain size. In the case of Ni/Cr(50), thinner individual layers would allow quicker access to oxygen, hence resulting in a larger percent increase of coating thickness for Ni/Cr(50).

Overall, the hardness and modulus of the aged coatings are similar to those found in the literature. Very shallow indents showed compliant behavior as smaller spinel particles came into direct contact with the probe tip. This indicates a loosely packed oxide on the topmost surface with a harder oxide layer beneath (CrO), as confirmed in the EDS mapping results (Sec. II B). Therefore, very low loads could not be used to measure the coating properties.

D. Microscratch

High-load scratch was performed on each coating sample to identify the parameters at the initiation of coating failure. Using a load range of 400–1200 mN, ramp load scratch experiments were performed, and the *in situ* normal displacement and *in situ* friction were measured vs the lateral displacement (fixed length of 100 μm). The scratch is used to extract P_c (critical load) and d_c (critical width) at the onset of failure to obtain the adhesion strength σ_a and shear strength τ_c of the coatings. Equation (4)

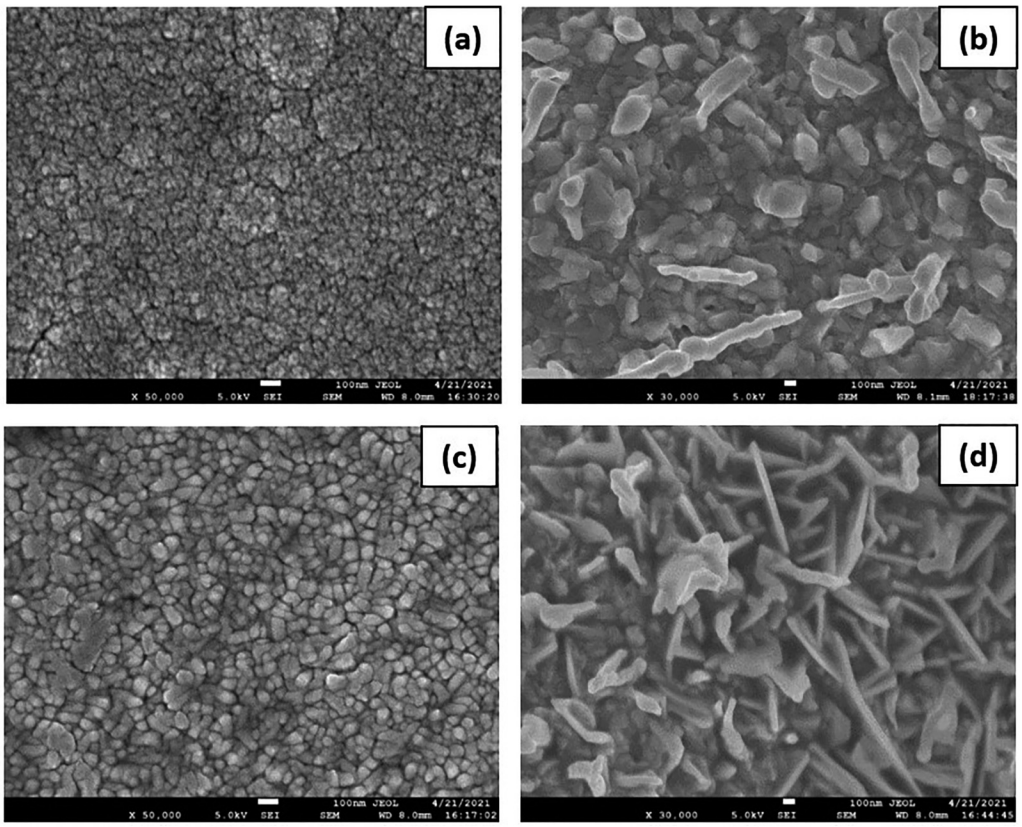

FIG. 7. Surface SEM of coatings (a) Ni/Cr(50)-RT, (b) Ni/Cr(50)-aged, (c) Ni/Cr(200)-RT, and (d) Ni/Cr(200)-aged.

shows how the adhesive strength (σ_a) can be calculated based on Laugier,[15]

$$\text{Adhesive Strength } (\sigma_a) = \frac{2P_c}{\pi d_c^2}\left[(4+\nu_s)\frac{3\pi\mu}{8} - (1-2\nu_s)\right]. \quad (4)$$

The adhesion strength σ_a is a function of the critical contact load (P_c) needed to delaminate the film from the substrate, residual width of the scratch (d_c) measured through SEM images, COF obtained from the experiment (μ) at the onset of delamination, and the substrate Poisson's ratio (ν_s) of 0.30. The critical load is determined by a combination of measuring the *in situ* depth, friction, as well as failure of the coatings under a microscope to assess the type of damage. The shear strength is also calculated using the critical load (P_c) value in addition to the hardness extracted from nanoindentation and the radius of the probe $r = 9.98\,\mu$m. It was determined by Benjamin and Weaver[16] and Ashcroft and Derby[17] that shear force per unit area (τ_c) can be written as a function of (H), (P_c), and (r) using Eq. (5),

$$\text{Shear Strength}(\tau_c) = \sqrt{\frac{HP_c}{\pi\left(r^2 - \frac{P_c}{\pi H}\right)}}. \quad (5)$$

TABLE I. Samples and nanoindentation material properties.

	Layer thickness (nm)	Total thickness (μm)	R_{rms} (nm)	E_r (GPa)	H (GPa)
Pure Ni	1000	1.0	20.0	132.9 ± 29.3	2.1 ± 0.7
Pure Cr	1000	1.0	3.0	153.9 ± 6.8	5.4 ± 0. 6
Ni/Cr(50)-RT	50	1.4	6.5	146.6 ± 10.3	6.6 ± 0.9
Ni/Cr(50)-aged	…	2–4	70.0	215.3 ± 28.8	14.2 ± 2.9
Ni/Cr(200)-RT	200	2.0	11.0	178.6 ± 3.8	5.9 ± 0.1
Ni/Cr(200)-aged	…	3–4	65.6	213.5 ± 38.5	14.4 ± 2.1

TABLE II. Adhesion and shear strength properties extracted from ramp load scratch.

	P_c (mN)	d_c (μm)	μ	σ_a (GPa)	τ_c (GPa)
Ni/Cr(50)-RT	220	10.0	0.35	1.34	2.28
Ni/Cr(50)-aged	300	9.8	0.40	3.23	4.65
Ni/Cr(200)-RT	290	11.4	0.60	3.78	2.57
Ni/Cr(200)-aged	380	11.5	0.47	3.28	4.34

It can be a challenge to determine the point of failure in case of ductile coating behavior. In this study, the pristine coatings are metallic and are expected to have ductile failure while the oxide after aging is expected to behave as a brittle material. However, the observed failure was different due to the nanocomposite multilayer system of the pristine coatings. Looking at the literature aimed to study failure of ductile coating responses, it can be seen that the point of failure can be identified by considering a number of factors. There can be an obvious transition in the trend of the COF, abrupt changes in depth of penetration (normal displacement), and finally, physical indications of failure other than immediate brittle crack and delamination. The indicators of failure from the scratch images are discussed by Bull *et al.* including parabolic cracks inside the scratch and spallation that was also seen for ductile materials.[18] They describe tensile and conformal cracking due to tension at the trailing edge of the indenter as part of ductile scratch failure, which results in parabolic scratches inside the scratch track. It was reported that in some cases ductile materials such as stainless steel can also show brittle failure. Particularly for ductile coatings, failure during scratch was investigated by Frey *et al.* as transitions in observed friction behavior by monitoring normal load during experiments.[19] For ductile materials, failure occurs if friction transition (abrupt spike in COF or a sudden change of slope of COF) is noticed along with observable features on the scratch surface such as cracks propagating inside or outside the scratch or spalled material pileup. A schematic has been added (Fig. S2 in the supplementary material) to show the types of scratch failures in samples.

Table II summarizes the adhesion and shear strength values obtained for these samples. The parameters for these calculations are extracted from Figs. 8–11. The onset of failure was determined using the *in situ* normal displacement and *in situ* friction (Figs. 8 and 10), while also examining the SEM images (Figs. 9 and 11) of the scratch and critical regions. The initiation of coating failure is identified as a combination of a sudden or large increase in friction force or large increase in displacement and visible increase in scratch damage.[10] For brittle coatings, failure is visible with large removal of coating, whereas for ductile materials, the onset of delamination may not follow these observations. There is a possibility that the initial ductile behavior of the coating transitions to brittle failure or crack propagation that can also be observed as pop-in of normal displacement during scratch.[20] For adhesion and shear strength calculations to be applicable, only the spherical region of the scratch probe must be utilized. The geometry of the conospherical probe is as follows: the tip radius of curvature is 9.98 μm and the included angle is 85°, providing a penetration

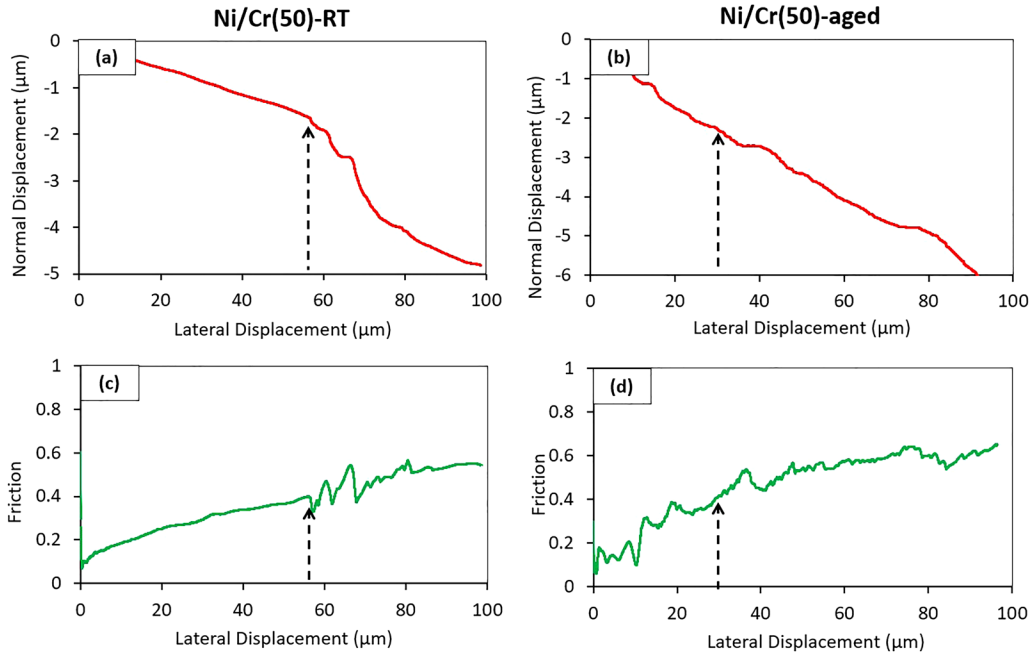

FIG. 8. Normal displacement and friction vs lateral displacement for (a) and (c) Ni/Cr(50)-RT and (b) and (d) Ni/Cr(50)-aged. The dashed arrows mark the points used for delamination parameters.

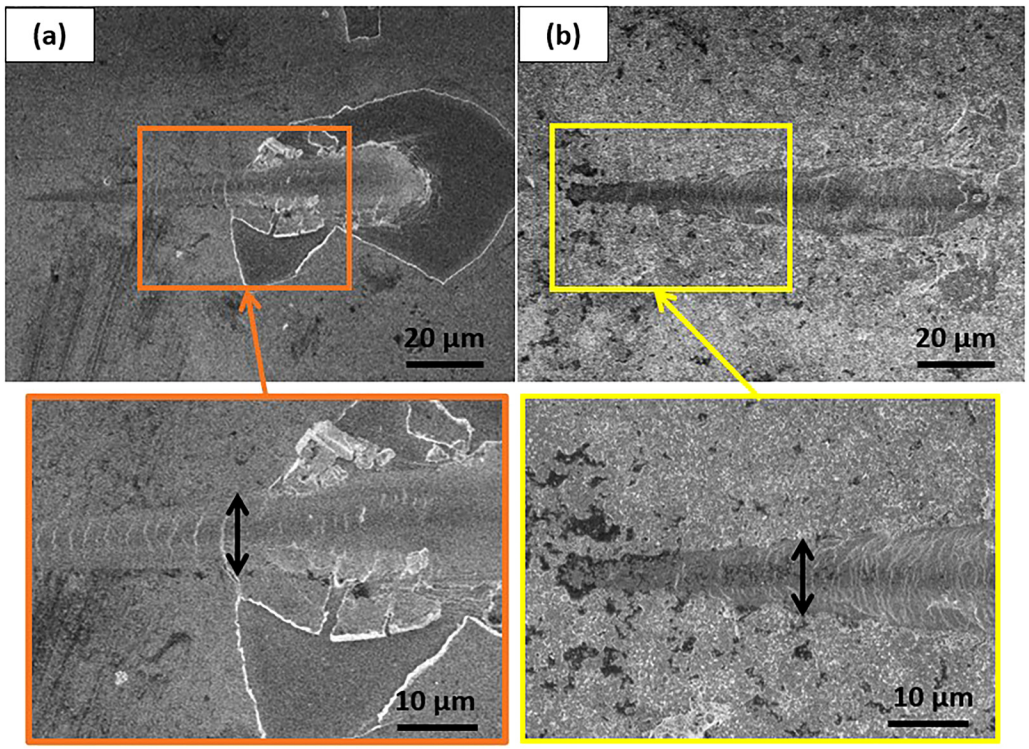

FIG. 9. SEM images of residual scratches used to measure critical width (a) Ni/Cr(50)-RT, (b) Ni/Cr(50)-aged, and magnified images. The point of failure is marked with a double arrow at higher magnification.

depth of 3.2 μm up to which the contact is purely in the spherical region. The depths of penetration should be less than or equal to 3.2 μm in the normal direction at which the adhesion and shear strengths are calculated. According to Figs. 8(a), 8(b), 10(a), and 10(b), the depths (at the point where P_c and d_c are extracted) are below 3.2 μm, hence the spherical part of the indenter is used.

The normal displacement and *in situ* friction vs the lateral scratch displacement are presented for Ni/Cr(50) in Fig. 8. In the case of these films, only Ni/Cr(50)-RT delaminated, indicating lower adhesion to the substrate as seen in Fig. 8(a) where an increase in normal displacement is evident after reaching 1.7 μm depth. The corresponding friction was extracted from Fig. 8(c). For aged Ni/Cr(50), the point of failure was more difficult to identify. The few initial pop-ins at low depth can be attributed to the spinel oxides on the surface and the porosity of the Cr oxide. The onset of failure was determined by performing a combined analysis with the SEM images where Fig. 9(b) indicated the region where the presence of parabolic microcracks have become more abundant, immediately after the chosen point of failure (marked with an arrow). Ni/Cr (50)-RT delaminates and exhibits the lowest adhesion strength of 1.34 GPa while aging increases adhesion strength significantly to 3.68 GPa as a result of the mixed oxide-rich coating with higher hardness (14 GPa) and good adherence to the Inconel substrate.

The shear strength also depends on the hardness and has shown improvement, increasing from 2.28 GPa [Ni/Cr(50)-RT] to 4.65 GPa after aging. Aging increases the adhesion to the substrate, preventing sudden detachment of the coating from the substrate and higher hardness enhanced the resistance to shear. The oxide layer has fused with the Inconel substrate hence failure is not as evident, and the material continues to undergo plastic deformation. A study involving deposited Cr_2O_3 on steel substrates has also exhibited excellent adhesion to the substrate along with favorable friction and wear behavior.[9]

Figure 10 shows the normal displacement and *in situ* friction for the Ni/Cr(200) samples. For the RT samples, initiation of failure is also difficult to ascertain. For the chosen point, the depth reached just beyond 2 μm, and the SEM images indicated a crack propagating from the sides of the scratch, Fig. 11(a). The Ni/Cr (200)-RT sample exhibited an adhesion strength of 3.78 GPa and shear strength of 2.57 GPa, both higher than that of Ni/Cr(50)-RT. For Ni/Cr(200)-aged, the determined point of failure is marked by a characteristic spike in friction, Fig. 10(d), observed in repeated scratch experiments. The SEM image in Fig. 11(b) also indicated an increased pileup in the region following the critical point on the scratch (marked with an arrow in the higher magnification). The aged sample of Ni/Cr(200) showed a similar adhesion strength value (3.28 GPa) to Ni/Cr(200)-RT and Ni/Cr(50)-aged. The calculated shear strength of Ni/Cr(200)-aged is 4.34 GPa, which is nearly double than that of the Ni/Cr(200)-RT sample showing the positive effect of aging.

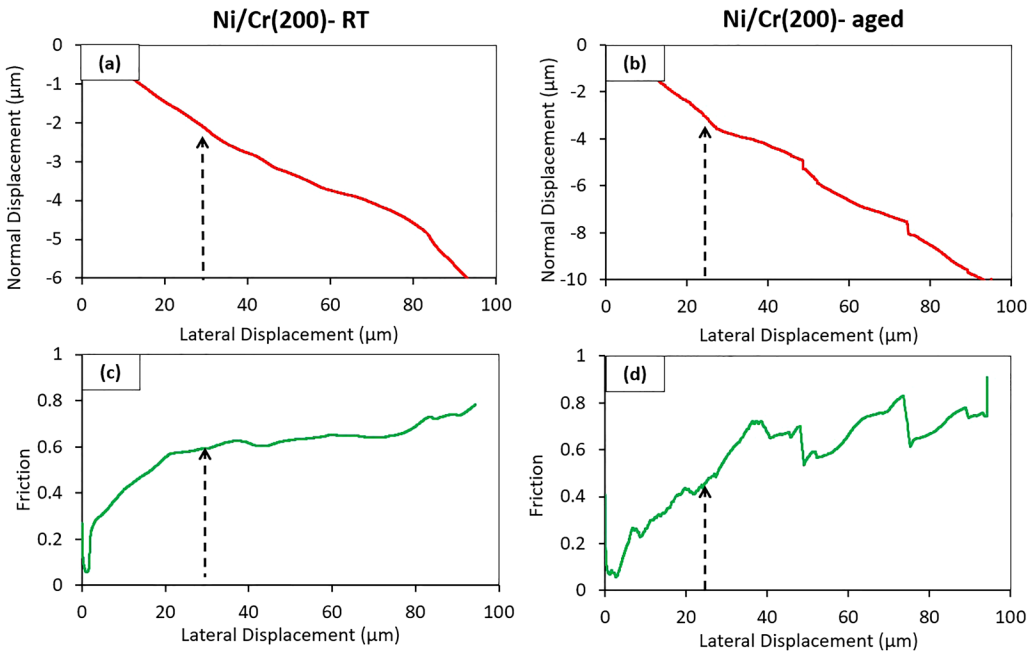

FIG. 10. Normal displacement and friction vs lateral displacement for (a) and (c) Ni/Cr(200)-RT and (b) and (d) Ni/Cr(200)-aged. The arrows mark the point used for delamination parameters.

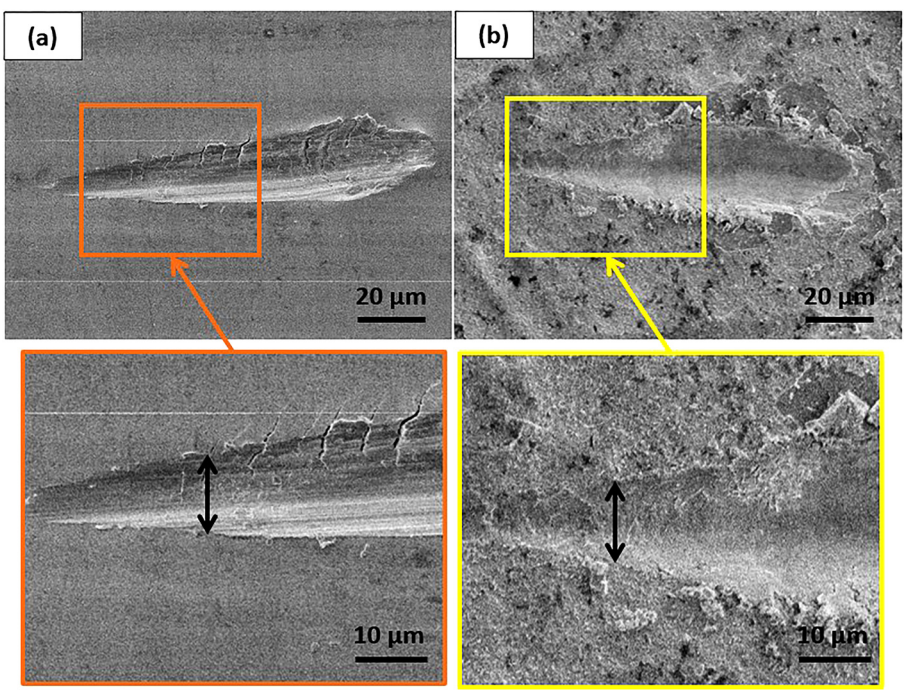

FIG. 11. SEM images of the residual scratches used to measure critical width (a) Ni/Cr(200)-RT and (b) Ni/Cr (200)-aged. The point of failure is marked with a double arrow at higher magnification.

It should be noted that residual stresses may arise in the oxide layers once cooled after the aging process. Residual stresses may affect the work due to adhesion but have no direct impact on the adhesive strength calculation (σ_a). In an earlier study, two different aged samples of Inconel with very similar oxide layers to the samples herein [Ni/Cr(50)-aged and Ni/Cr(200)-aged] were subjected to x-ray diffraction at various tilt angles.[21] The residual stresses calculated can then be used to obtain the total local stresses $\sigma_c = \sigma_a + \sigma_{in}$, where σ_{in} is the residual stresses and σ_a is the adhesive stress calculated using Laugier's method. Then, σ_{in} is added to the calculated value of σ_a at the critical point, and the resulting σ_c can be used to obtain the work of adhesion. It was reported that for such oxide coatings, having residual compressive stresses increased the work due to adhesion of both the samples investigated, with the observed trend being the same.

The only coating to delaminate completely is Ni/Cr(50)-RT, while Ni/Cr(200)-RT having thicker individual layers resisted delamination. The cohesion between the individual layers of Ni and Cr outweighs the adhesion strength with the Inconel substrate in the case of Ni/Cr(50)-RT. Any defect at the coating–substrate interface quickly delaminates the coating from that point onward. Aged samples show better shear strength due to higher hardness of the oxide layer, which is also strongly bonded to the Inconel. Overall, the scratch results support the macro-tribology results where Ni/Cr(50)-RT was the only delaminated coating. While the Ni/Cr(200) coatings (RT and aged) exhibited very similar wear loss after the experiments.

IV. CONCLUSIONS

Multilayer coatings of Ni and Cr deposited onto Inconel 617 and their physical properties were assessed using high temperature macro-tribological experiments, which were related to nanoindentation and microscratch experiments. These techniques were used to identify changes in coating hardness, film adhesion, and friction behavior, as a consequence of aging at very high temperatures. The following conclusions could be drawn.

The macro-tribology results showed that Ni/Cr(50)-RT was the only delaminated coating despite thinner individual layer thickness (50 nm). While Ni/Cr(200) with an individual layer thickness of 200 nm coatings (RT and aged) all exhibited similar minimal wear after the experiments. The Ni/Cr(200)-RT coating provides lower COF compared to pure Inconel 617 at 800 °C. Additionally, aging of both coatings caused a reduction of *in situ* COF. Moreover, wear and COF reduction are evident on RT samples tested at 800 °C, which underwent *in situ* aging and behaved similar to the aged samples.

- Nanoindentation data verified that the coatings exhibited higher indentation hardness (~6 GPa) than each of the individual constituents of Ni and Cr (when coated onto silicon substrates). After aging both coatings exhibited over 50% increase in hardness (~14 GPa).
- Ramp load microscratch results showed Ni/Cr(50)-RT to have the least resistance to delamination while aging improved the adhesion strength of Ni/Cr(50). Removal of Ni/Cr(50)-RT from the substrate indicated higher cohesion between Ni/Cr layers compared to adhesion to the Inconel substrate. Ni/Cr(200) samples showed higher shear strength after aging, whereas the adhesion strength did not change significantly.
- Cross-section EDS confirmed that the aged oxide layer is two to three times thicker than the originally deposited coating. Nickel migrates away from the coating and an abundance of chromium oxide gives the coatings higher hardness. The oxide layer is well bonded, resulting in low wear under high temperature tribology experiments and relatively smooth transition to the substrate when ramp scratch was performed.
- Both Ni/Cr coatings exhibit similar oxidation behavior to aged Inconel 617 studied previously. This indicates the potential of such coating to prevent aging and loss of Cr from the Inconel beneath. The Ni/Cr coating ages to provide a well-bonded CrO layer; however, the rate of aging is affected by the individual layer thickness.
- Due to the nanoscale thickness of the individual layers, it is expected that the tribological behavior could vary across scales. The multiscale analysis here provides some evidence that there is indeed a correlation of physical properties between macro-, micro-, and nanoscales.

SUPPLEMENTARY MATERIAL

See the supplementary material for depicting an SEM image of the coating surface of Ni/Cr(50) after testing at 800 °C (Fig. S1). Figure S2 is a schematic of different types of observed features on scratches upon failure.

ACKNOWLEDGMENTS

This study is supported by the U.S. Department of Energy (DOE) under Nuclear Energy University Program (NEUP) Project No. 16-10732 under Federal Grant No. DE-NE0008549. The authors also would like to thank Dr. J. Ding and Dr. X. Zhang of Purdue University for preparing the samples and providing the TEM image in Fig. 1. The use of Texas A&M University Materials Characterization Core Facility (No. RRID:SCR_022202) is acknowledged.

AUTHOR DECLARATIONS

Conflicts of Interest

The authors have no conflicts to disclose.

Author Contributions

Ayesha Asif: Conceptualization (equal); Data curation (equal); Formal analysis (equal); Methodology (equal); Validation (equal); Visualization (equal); Writing – original draft (equal). **Saifur Rahman:** Conceptualization (equal); Data curation (equal); Formal analysis (equal); Validation (equal); Visualization (equal); Writing – original draft (equal). **Andreas A. Polycarpou:** Conceptualization (equal); Funding acquisition (equal); Project administration (equal); Resources (equal); Supervision (equal); Writing – review & editing (equal).

DATA AVAILABILITY

The data that support the findings of this study are available from the corresponding author upon reasonable request.

REFERENCES

[1]A. Sáenz-Trevizo and A. M. Hodge, Nanotechnology **31**, 292002 (2020).
[2]K. Aouadi, C. Nouveau, A. Besnard, B. Tlili, A. Montagne, and M. Chafra, J. Mater. Eng. Perform. **30**, 2526 (2021).
[3]D. Kim, I. Sah, D. Kim, W.-S. Ryu, and C. Jang, Oxid. Met. **75**, 103 (2011).
[4]C. Jang, D. Kim, D. Kim, I. Sah, W.-S. Ryu, and Y.-S. Yoo, Trans. Nonferr. Met. Soc. China **21**, 1524 (2011).
[5]D. Kim, C. Jang, and W. S. Ryu, Oxid. Met. **71**, 271 (2009).
[6]W.-J. Shong, C.-K. Liu, S.-H. Wu, H.-C. Liu, and P. Yang, Int. J. Hydrogen Energy **39**, 19737 (2014).
[7]M. S. Rahman, J. Ding, A. Beheshti, X. Zhang, and A. A. Polycarpou, Tribol. Int. **123**, 372 (2018).
[8]M. S. Rahman, K. Polychronopoulou, and A. A. Polycarpou, Wear **462–463**, 203508 (2020).
[9]H. Liu, J. Tao, J. Xu, Z. Chen, and Q. Gao, Surf. Coat. Technol. **204**, 28 (2009).
[10]J. Lee, K. Polychronopoulou, A. N. Cloud, J. R. Abelson, and A. A. Polycarpou, Wear **318**, 168 (2014).
[11]M. S. Rahman, K. Polychronopoulou, and A. A. Polycarpou, J. Nucl. Mater. **521**, 21 (2019).
[12]W. C. Oliver and G. M. Pharr, J. Mater. Res. **7**, 1564 (1992).
[13]S. Yoshida, T. Bhattacharjee, Y. Bai, and N. Tsuji, Scr. Mater. **134**, 33 (2017).
[14]T. Jõgiaas, A. Tarre, H. Mändar, J. Kozlova, and A. Tamm, Nanomaterials **12**, 82 (2022).
[15]M. T. Laugier, Thin Solid Films **117**, 243 (1984).
[16]P. Benjamin and C. Weaver, "Adhesion of metal films to glass," Proc. R. Soc. Lond., A **254**(1277), 177–183 (1960).
[17]I. A. Ashcroft and B. Derby, J. Mater. Sci. **28**, 2989 (1993).
[18]S. J. Bull, Surf. Coat. Technol. **50**, 25 (1991).
[19]N. Frey, P. Mettraux, G. Zambelli, and D. Landolt, Surf. Coat. Technol. **63**, 167 (1994).
[20]X. Xiao, J. Deng, Q. Xiong, Q. Yan, Z. Wu, and H. Lin, Micromachines **12**, 707 (2021).
[21]M. S. Rahman and A. A. Polycarpou, J. Mater. Res. **37**, 580 (2022).